

Effective boundary conditions for transpiration cooling applications

Valentina König and Siegfried Müller

Institut für Geometrie und Praktische Mathematik
Templergraben 55, 52062 Aachen, Germany

Effective boundary conditions for transpiration cooling applications

By V. König AND S. Müller

Institut für Geometrie und Praktische Mathematik, RWTH Aachen University
Templergraben 55, 52056 Aachen

Transpiration cooling is numerically investigated, where a cooling gas is injected through a carbon composite material into a hot gas channel. To simulate this process efficiently an effective problem is derived, where effects induced by micro-scale structures on macro-scale variables, e.g. cooling efficiency, are taken into account without resolving the micro-scale structures. The key idea of the effective model is to determine effective boundary conditions at the interface between hot gas and porous medium flow. These are derived using an upscaling strategy. Numerical simulations in 2D with effective boundary conditions are compared with results obtained from computations with uniform and non-uniform injection. The computations confirm that the effective model provides a better approximation of the cooling efficiency than the uniform injection.

1. Introduction

To simulate transpiration cooling the process of a cooling gas entering a hot gas flow through a porous material needs to be modeled. The problem at hand is a channel with a hot gas flow. Mounted into the wall of the channel is a porous material. A reservoir containing the cooling gas is attached to the porous material.

Compared with other active cooling techniques such as film or effusion cooling, transpiration cooling might offer advantages regarding the formation of stable films, see Linn et al. [1, 2] and Linn et al. [3], and the cooling efficiency. With the availability of permeable ceramics, in particular composite carbon/carbon materials, investigated for instance by Selzer et al. [4], the development of transpiration-cooled combustion chambers is a recent research topic, see for instance Ortelt et al. [5] or Herbertz et al. [6]. Numerical simulations of hot gas flows exposed to transpiration cooling were conducted by Jiang et al. [7] and more recently by Liu et al. [8]. The objective of these simulations was the investigation of the effect of the cooling gas injection on the hot gas flow, especially on the boundary layer.

Injecting cooling gas through a porous medium into a hot gas channel flow was numerically investigated in [9] and [10] using a two-domain approach. Here, the injection was modeled uniformly, i.e. all roughness scales are neglected. In [11] to simulate non-uniform injection the two-domain approach was extended by taking measured interface outflow distributions into account. The results validated by experimental data confirmed the assumption that micro-scale effects, e.g. local mass fluxes, have significant influence on the macro-scale behavior of the cooling effect, such as the cooling film shape or cooling efficiency. Computations at the interface on the pore scale using reconstruction methods are presented in [12].

The turbulent channel flow and the flow within the pore-scale tubes in the porous material can be described by the Navier-Stokes equations. A direct numerical simulation (DNS), i.e., resolution of all scales, of the hot gas flow in the channel and the porous medium flow is not feasible due to the tremendous computational effort. In [13] the pore scale for a uniform (coarse) pore distribution was discretized to analyze the effect on the velocity. Applying well established averaging models like RANS for the hot gas flow and Darcy-based models for the porous medium flow help understand general effects of transpiration cooling on the macro-scale at an affordable cost.

Our goal is the development of a new method that combines the advantages of an affordable averaged macro-scale computation with information from the micro-scale. Here the micro-scale effects that have an impact on macro-scale values are of special interest. In terms of transpiration cooling we would like to analyze how the rough porous injection interface affects the cooling film or the cooling efficiency in the turbulent channel flow.

While passing through the porous material the cooling gas is transported through microscopic channels that form the void space in the porous structure. At the interface the cooling gas is therefore entering the channel flow through microscopic pores. The distribution of the pores is assumed to have an influence on the development of a cooling film.

Typically the effects of the pore-scale (micro-scale) injection at the interface towards the hot gas flow are neglected in averaged models. Experiments performed in a wind tunnel at the ITLR Stuttgart show that these micro-scale effects have a significant influence on the behavior of the cooling film [11]. For a better understanding of the micro-scale influence at the coupling interface on macro-scale quantities we develop a macro-scale model that takes micro-scale effects at the interface into account without resolving the entire micro-scale. This is done by deriving effective boundary conditions using an up-scaling strategy motivated by the strategy presented in [14].

Derivations of effective boundary conditions for parallel porous medium flow can be found in [15]. A rigorous analytical derivation is presented in [16] also for parallel porous flow. In [17] this approach was used to determine boundary conditions for flows that enter the porous material at the interface. In our case the cooling gas is injected into the hot gas flow and therefore exits the porous material at the interface. In [18] effective interfacial velocity boundary conditions based on the Stokes equations were derived. Since in our setting we are interested in the heat transfer, our derivation is based on the Navier-Stokes equations.

The physical model of the subsonic channel flow and the porous medium flow as well as the uniform coupling of the two solvers are briefly summarized in Sec. 2.1. In Sec. 2.2 we introduce the micro-scale interface problem. The arising effective macro-scale model is presented in Sec. 2.3. In Sec. 3, the derivation of effective boundary conditions is described. Both the experimental and numerical setup as well as the numerical results of all components leading to an effective computation are presented in Sec. 4. A summary of the main results in Sec. 5 concludes the paper.

2. Mathematical modeling

To develop a macro-scale model that takes micro-scale effects at the interface into account we first summarize the established two-domain approach, see [9, 10], for uniform

injection in Sec. 2.1. Then we introduce a so-called micro-scale interface problem in Sec. 2.2, where we pay special attention to the interface. This problem is derived using the established two-domain approach for uniform injection. Finally, the micro-scale interface problem is used to derive a so-called effective model in Sec. 2.3, where the effects of the micro-scale at the interface are incorporated without resolving the micro-scale pores.

2.1. Zeroth-order problem

The zeroth-order problem, developed in [9], is a two-domain approach with the domains Ω_{HG} and Ω_{PM} for the hot gas flow and the porous medium, respectively, see Figure 1, that does not account for micro-scale effects at the coupling interface. In the following, we summarize the governing equations and boundary as well as coupling conditions for these domains.

2.1.1. Hot gas domain Ω_{HG}

The channel hot gas flow is modeled using Favre-averaged RANS-equations closed by the Wilcox k - ω turbulence model [19]:

$$\nabla \cdot (\bar{\rho} \tilde{\mathbf{v}}) = 0, \quad (2.1)$$

$$\nabla \cdot (\bar{\rho} \tilde{\mathbf{v}} \otimes \tilde{\mathbf{v}} + \bar{p} \mathbf{I}) = \nabla \cdot (\bar{\boldsymbol{\tau}} + \bar{\rho} \tilde{\mathbf{R}}), \quad (2.2)$$

$$\nabla \cdot (\tilde{\mathbf{v}}(\bar{\rho} \tilde{E} + \bar{p})) = \nabla \cdot \left((\bar{\boldsymbol{\tau}} + \bar{\rho} \tilde{\mathbf{R}}) \tilde{\mathbf{v}} - \bar{\mathbf{q}} + \bar{\mathbf{q}}^t + \overline{\mathbf{v}'' \boldsymbol{\tau}} - \frac{1}{2} \overline{\rho (\mathbf{v}'')^2 \mathbf{v}''} \right), \quad (2.3)$$

$$\nabla \cdot (\bar{\rho} \tilde{\mathbf{v}} \tilde{k}) = \bar{\rho} \sum_{i,j} \tilde{R}_{ij} \frac{\partial \tilde{v}_i}{\partial x_j} - \beta^* \bar{\rho} \tilde{k} \tilde{\omega} + \nabla \cdot \left(\left(\mu + \sigma^* \frac{\bar{\rho} \tilde{k}}{\tilde{\omega}} \right) \nabla \tilde{k} \right), \quad (2.4)$$

$$\nabla \cdot (\bar{\rho} \tilde{\mathbf{v}} \tilde{\omega}) = \alpha \frac{\tilde{\omega}}{\tilde{k}} \bar{\rho} \sum_{i,j} \tilde{R}_{ij} \frac{\partial \tilde{v}_i}{\partial x_j} - \beta \bar{\rho} \tilde{\omega}^2 + \sigma_d \frac{\bar{\rho}}{\tilde{\omega}} \nabla \tilde{k} \nabla \tilde{\omega} + \nabla \cdot \left(\left(\mu + \sigma \frac{\bar{\rho} \tilde{k}}{\tilde{\omega}} \right) \nabla \tilde{\omega} \right). \quad (2.5)$$

Here, $\tilde{(\cdot)}$ denotes the Favre-averaged and $\bar{(\cdot)}$ the Reynolds-averaged values. This system is solved for the conservative flow quantities

$$\mathbf{U}_{HG} = \left(\bar{\rho}, \bar{\rho} \tilde{\mathbf{v}}, \bar{\rho} \tilde{E}, \bar{\rho} \tilde{k}, \bar{\rho} \tilde{\omega} \right), \quad (2.6)$$

where $\bar{\rho}$ is the density, $\tilde{\mathbf{v}}$ the fluid velocity vector, \tilde{k} the turbulent kinetic energy and $\tilde{\omega}$ the specific dissipation rate. The total energy \tilde{E} is given by $\tilde{E} = \tilde{e} + 1/2 \tilde{\mathbf{v}}^2$ with the specific internal energy \tilde{e} . While the components of the mean viscous stress tensor $\bar{\boldsymbol{\tau}}$ are computed directly, the Reynolds stress tensor $\bar{\rho} \tilde{\mathbf{R}}$ is modeled via the Boussinesq hypothesis [20]. The mean heat flux $\bar{\mathbf{q}}$ is computed applying Fourier's law, i.e.,

$$\bar{\mathbf{q}} = -c_p \frac{\mu}{Pr} \nabla \bar{T}, \quad (2.7)$$

where c_p is the specific heat capacity at constant pressure, μ the dynamic viscosity, Pr the Prandtl number and \bar{T} the mean temperature. Accordingly, the mean turbulent heat flux is modeled by

$$\bar{\mathbf{q}}^t = -c_p \frac{\mu_t}{Pr_t} \nabla \bar{T} \quad (2.8)$$

with the turbulent Prandtl number set to $Pr_t = 0.9$. The turbulent viscosity μ_t is modeled by Wilcox's turbulence model. The diffusion of the turbulent kinetic energy described by $\nabla \cdot \left(\overline{\mathbf{v}'' \boldsymbol{\tau}} - \frac{1}{2} \overline{\rho (\mathbf{v}'')^2 \mathbf{v}''} \right)$ in the energy equation (2.3) is neglected. For the closure of the

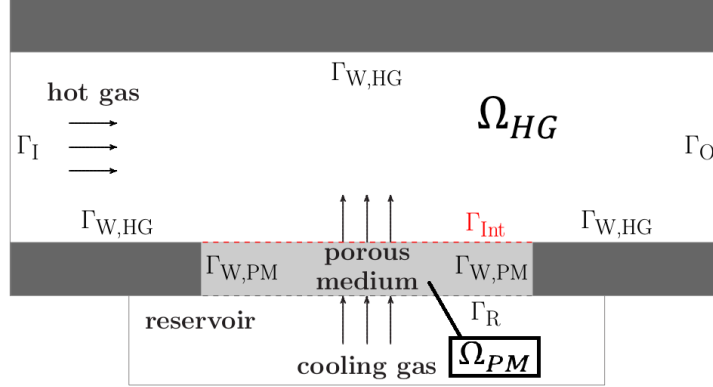


FIGURE 1. Transpiration cooling setup for zeroth-order problem.

system, we use the equation of state for a thermally and calorically perfect gas

$$\bar{p} = \bar{\rho} R \bar{T}. \quad (2.9)$$

The specific gas constant R is determined by $R = (\gamma - 1) c_p / \gamma$ with the isentropic exponent γ . We refer to [19] for detailed information on the turbulence model and the choice of the coefficients β^* , σ^* , α , β , σ_d and σ . In the following, we omit the labeling of averaged quantities ($\bar{(\cdot)}$ or (\cdot)).

The system (2.1) - (2.5) has to be complemented by suitable boundary conditions for the configuration in Figure 1. Here, we discuss the conditions for a subsonic hot gas flow. At the inflow boundary Γ_I , the velocity and the temperature are prescribed by

$$\mathbf{v} = \mathbf{v}_\infty, \quad T = T_\infty \quad \text{on } \Gamma_I, \quad (2.10)$$

where the subscript ∞ indicates the inflow conditions. The static pressure on Γ_I is extrapolated from the interior flow domain.

At the outflow boundary Γ_O , only the pressure is prescribed by setting

$$p = p_\infty \quad \text{on } \Gamma_O. \quad (2.11)$$

For the walls $\Gamma_{W,HG}$ of the channel we use adiabatic walls to account for the changing wall temperature due to the cooling.

2.1.2. Porous medium domain Ω_{PM}

The porous medium flow is characterized by the porosity φ of the material, i.e., the ratio of the void space to the total volume of the medium. We assume that the entire void space is connected. Thus, we do not have to deal with isolated cavities. Furthermore, the porosity is constant in the entire domain.

In [21] the relation $\mathbf{v} = \varphi \mathbf{V}$ between the intrinsic average velocity \mathbf{V} and the Darcy velocity \mathbf{v} is introduced. The average velocity \mathbf{V} is obtained by averaging the fluid velocity over a volume that consists of fluid only. The Darcy velocity \mathbf{v} , also known as seepage or filtration velocity, is the average velocity over a volume that incorporates both, solid and fluid material.

The flow through the porous material on Ω_{PM} is described by:

$$\nabla \cdot (\rho_f \mathbf{v}) = 0, \quad (2.12)$$

$$\rho_f \varphi^{-2} (\mathbf{v} \cdot \nabla) \mathbf{v} = -\nabla P - \frac{\mu}{K_D} \mathbf{v} - \frac{\rho_f}{K_F} \|\mathbf{v}\|_2 \mathbf{v}, \quad (2.13)$$

$$(\varphi - 1)\nabla \cdot (\boldsymbol{\kappa}_s \nabla T_s) = h_v (T_f - T_s), \quad (2.14)$$

$$\rho_f c_{p,f} \mathbf{v} \cdot \nabla T_f - \varphi \nabla \cdot (\boldsymbol{\kappa}_f \nabla T_f) = h_v (T_s - T_f). \quad (2.15)$$

This system is solved for the variables

$$\mathbf{U}_{PM} = (\rho_f, \mathbf{v}, T_s, T_f) \quad (2.16)$$

which denote the fluid density, the Darcy velocity, the solid temperature and the fluid temperature, respectively.

The continuity equation (2.12) implies mass conservation and describes the behavior of the fluid density in the porous media. We consider the Darcy-Forchheimer equation (2.13) to incorporate the conservation of momentum and to model the pressure gradient driven flow through the porous material. The temperature of the solid and the fluid are assumed to be in non-equilibrium. Therefore we need two heat equations (2.14) and (2.15). Here, μ denotes the dynamic viscosity of the fluid, K_D the permeability coefficient of the medium, K_F the Forchheimer coefficient, $c_{p,f}$ the heat capacity of the fluid and h_v the heat transfer coefficient. The heat conduction tensor of the solid $\boldsymbol{\kappa}_s$ consists of a component for the parallel flow direction $\kappa_{s,par}$ and for normal flow direction $\kappa_{s,nor}$, respectively:

$$\boldsymbol{\kappa}_s = \begin{bmatrix} \kappa_{s,nor} & 0 \\ 0 & \kappa_{s,par} \end{bmatrix} \quad (2.17)$$

For the heat conduction coefficient of the fluid $\kappa_f = c_{p,f} \mu / Pr$ the dynamic viscosity μ is computed using Sutherland's law.

Again to close the system we use the ideal gas equation for the pressure

$$P = \rho_f T_f R \quad (2.18)$$

with R being the specific gas constant.

Assuming that the conditions in the reservoir are constant and homogeneous we can derive the pressure and the temperatures on the reservoir boundary by measuring the coolant temperature T_c and the pressure P_c . Furthermore let T_b be the temperature of the solid on the backside of the porous material. Then the boundary conditions on the reservoir boundary read

$$P = P_c, \quad T_s = T_b, \quad T_f = T_c \quad \text{on } \Gamma_R. \quad (2.19)$$

Since the fluid density can be computed by the ideal gas law we get

$$\rho_R := \rho = \frac{P_c}{RT_f} \quad \text{on } \Gamma_R. \quad (2.20)$$

We assume the solid side walls at $\Gamma_{W,PM}$ to be adiabatic, i.e.,

$$\nabla T_s \cdot \mathbf{n} = 0, \quad \nabla T_f \cdot \mathbf{n} = 0 \quad \text{on } \Gamma_{W,PM} \quad (2.21)$$

and the slip-conditions to hold, i.e.,

$$\mathbf{n} \cdot \mathbf{v} = 0 \quad \text{on } \Gamma_{W,PM}, \quad (2.22)$$

because viscous effects are neglected in Equations (2.12) and (2.13), i.e., the attached flow is parallel to $\Gamma_{W,PM}$. Thus, the normal velocity component must vanish, whereas non-trivial tangential velocity components have to be permitted. Therefore Equations (2.12) and (2.13) need characteristic boundary conditions on $\Gamma_{W,PM}$. The nonlinear term in (2.13) allows the velocity \mathbf{v} to match to a physically correct tangential field at

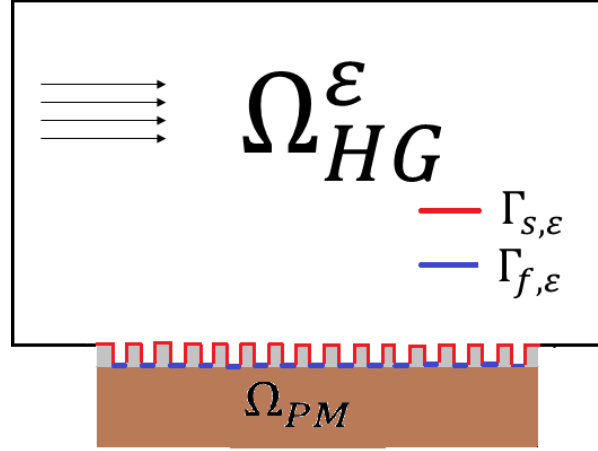


FIGURE 2. Micro-scale interface problem.

$\Gamma_{W,PM}$. This also implies a characteristic boundary $\Gamma_{W,PM}$ for Equation (2.12), i.e., in our case no boundary conditions for the density ρ have to be imposed.

2.1.3. Macro-scale coupling conditions at Γ_{Int}

At the smooth interface Γ_{Int} coupling conditions for the hot gas domain Ω_{HG} consist of

$$\rho = \frac{p}{RT_{f,PM}}, \quad \mathbf{v} = \mathbf{v}_{PM}, \quad E = c_v T_{f,PM} + \frac{1}{2} |\mathbf{v}_{PM}|^2. \quad (2.23)$$

The values for the pressure p and the density ρ in (2.23) and for the friction velocity u_τ and the dynamic viscosity μ in (2.24) below are determined by the hot gas flow. The temperature $T_{f,PM}$ and the velocity \mathbf{v}_{PM} of the fluid are provided by the porous medium flow. The turbulent kinetic energy at the interface is set to zero. To account for mass injection at the modeled porous surface the specific dissipation rate is set to

$$\omega = \frac{\rho u_\tau^2}{\mu} \frac{25}{\frac{v_{2,PM}}{u_\tau} \left(1 + 5 \frac{v_{2,PM}}{u_\tau}\right)}, \quad (2.24)$$

where $v_{2,PM}$ denotes the velocity component normal to the interface and $u_\tau = \sqrt{\tau_w / \rho}$ the friction velocity with the wall shear stress τ_w . For Ω_{PM} the coupling conditions at the interface Γ_{Int} consist of

$$v_2 = \frac{\dot{m}_c}{\rho_{mix} A_c} \quad \text{with} \quad \rho_{mix} = \frac{p_{HG}}{T_f R}, \quad (2.25)$$

where \dot{m}_c denotes the coolant mass flow rate and A_c the surface area of the porous medium, and

$$(1 - \varphi) (\boldsymbol{\kappa}_s \nabla T_s) \cdot \mathbf{n} = c_{p,f} \rho_f v_y (T_f - T_{HG}) + \kappa \nabla T_{HG} \cdot \mathbf{n}. \quad (2.26)$$

Here, information from the hot gas flow enter using the hot gas pressure p_{HG} , the temperature T_{HG} and the heat flux $\kappa \nabla T_{HG}$ with the hot gas heat conduction coefficient κ .

2.2. Micro-scale interface model

The zeroth-order problem does not account for micro-scale effects at the coupling interface but a uniform mass flow rate \dot{m}_c is assumed in the coupling conditions (2.25). To account for these effects we want to derive effective coupling conditions. For this purpose we introduce a micro-scale interface model. The micro-scale is active only at the injection interface, because the roughness of the porous material directly affects the cooling film in the hot gas channel. Hence, the domain Ω_{HG} is extended to Ω_{HG}^ε , see Figure 2.

The roughness is assumed to be periodic, i.e., the rough interface Γ_{Int}^ε between Ω_{HG}^ε and Ω_{PM} is composed of periodic roughness elements. Each element can be considered as an idealized pore consisting of an injection channel and the surrounding solid structure, see Figure 3(right). Here, d_S is the diameter of the solid wall separating two channels, see Figure 3(left). Thus, one element of size ε consists of solid structure and void space (injection channel). To ensure that the ratio of the injection channel volume related to the whole volume of the element is still φ we choose

$$\varepsilon = \frac{d_S}{(1 - \varphi)}. \quad (2.27)$$

Following [4], for a given porosity φ and permeability K_D of a porous material, both measured in experiments, the diameter of the small solid wall d_S is here determined by using the Ergun approach [22]:

$$K_D = \frac{\varphi^3 d_S^2}{150(1 - \varphi)^2}. \quad (2.28)$$

Note that in the original Ergun equation d_S denotes the particle diameter of the porous bed. This should be kept in mind for application purposes.

Following the zeroth-order problem in Sec. 2.1, the flow in the hot gas channel is modeled using RANS equations and the boundary conditions at Γ_I , Γ_O and $\Gamma_{W,HG}$ are chosen as presented in Sec. 2.1.1. In contrast to the zeroth-order problem there is no interface Γ_{Int} , but the interface to the porous material $\Gamma_{Int}^\varepsilon = \Gamma_{s,\varepsilon} \cup \Gamma_{f,\varepsilon}$ now consists of solid walls $\Gamma_{s,\varepsilon}$ and channel entries $\Gamma_{f,\varepsilon}$. We assume the solid walls to be isothermal, i.e.,

$$T = T_{s,PM} \quad \text{on } \Gamma_{s,\varepsilon} \quad (2.29)$$

and the no-slip-conditions to hold, i.e.,

$$\mathbf{v} = \mathbf{0} \quad \text{on } \Gamma_{s,\varepsilon}. \quad (2.30)$$

For the inflow conditions at $\Gamma_{f,\varepsilon}$ we need to adjust the coupling conditions of the zeroth-order problem to ensure the conservation of momentum. The latter is not present in the zeroth-order problem due to the averaged velocity over the entire interface. Because of the split of the interface into solid walls and microscopic injection channels we have to use the intrinsic average velocity $\mathbf{V} = \mathbf{v}/\varphi$ at $\Gamma_{f,\varepsilon}$:

$$\rho = \frac{p}{RT_{f,PM}}, \quad \mathbf{V} = \frac{\mathbf{v}_{PM}}{\varphi}, \quad E = c_v T_{f,PM} + \frac{1}{2} |\mathbf{V}|^2.$$

The flow through microscopic injection channels is assumed to be laminar, because in our setting the pore Reynolds number in the porous medium flow is small. Note that the flow in the injection channels is not characterized by the Reynolds number of the hot gas flow.

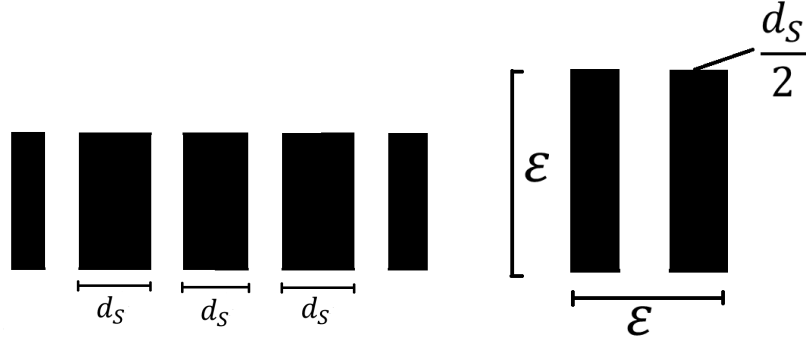


FIGURE 3. Zoom into the micro-scale modeled interface(left), configuration depending on ε (right).

For the micro-scale interface model it holds $\Omega_{HG}^\varepsilon \supset \Omega_{HG}$. With $\varepsilon \rightarrow 0$ the roughness elements become smaller but their number increases to infinity and the micro-scale interface Γ_{Int}^ε approaches the interface Γ_{Int} of the zeroth-order problem. Thus, in the limit we tend to a uniform injection along the entire porous sample that coincides with the zeroth-order approach.

2.3. Effective macro-scale model

Micro-scale effects arising from the roughness are neglected in the two-domain approach in Sec. 2.1. On the other hand, solving the micro-scale interface problem in Sec. 2.2 is very expensive and therefore not feasible. For instance, for the 3-D computations performed in [11] the grid would need to resolve over 40,000 microscopic injection channels for a sample of "only" $48\text{mm} \times 48\text{mm}$. Hence, we develop a concept that improves the zeroth-order model without resolving each microscopic pore channel at the hot gas interface. The strategy is to derive so-called effective boundary conditions for the hot gas flow using an upscaling technique.

Numerical investigations presented in [10] using the two-domain approach in Sec. 2.1 confirmed that there is a significant effect on the boundary layer in the hot gas flow near the interface, but not far away from it. Therefore solving the zeroth-order model gives a first approximation to simulate a transpiration cooled channel. The idea is to upscale the flow field in the hot gas domain obtained by the two-domain approach using effective boundary conditions at the interface Γ_{Int} . Note, that we do not couple the hot gas domain with the porous medium domain, because we assume that the effective conditions have almost no effect on the porous medium flow. Thus, the flow is modeled again using RANS equations and the boundary conditions at Γ_I , Γ_O and $\Gamma_{W,HG}$ are chosen as presented in Sec. 2.1.1. We replace the boundary conditions (2.23) at the interface Γ_{Int} with effective injection boundary conditions:

$$\rho = \frac{p}{RT^{eff}}, \quad \mathbf{v} = \mathbf{v}^{eff}, \quad E = c_v T^{eff} + \frac{1}{2} |\mathbf{v}^{eff}|^2.$$

The values for the temperature T^{eff} and the velocity \mathbf{v}^{eff} accounting for the effects of the micro-scale interface model on Ω_{HG}^ε are derived in Sec. 3.3. In particular, the

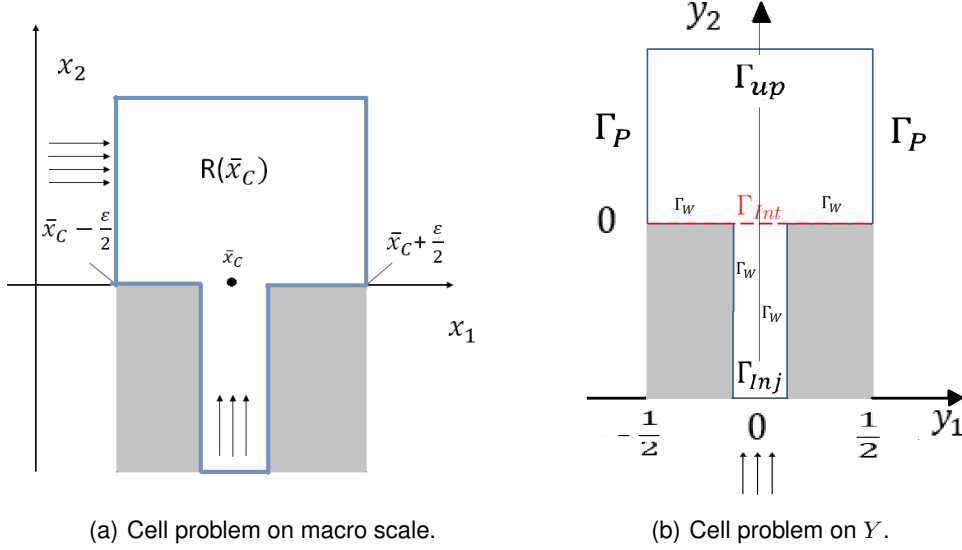


FIGURE 4. Cell problem on both scales.

effective boundary conditions have to ensure the correct mass flow rate entering the hot gas channel flow.

3. Derivation of effective boundary conditions

In the original two-domain approach in Sec. 2.1 the cooling gas is uniformly injected into the hot gas channel flow. The roughness of the porous material and the geometry of the channel distribution do not directly enter this model. To derive boundary conditions that capture the effects of the roughness on the hot gas channel flow as modeled in the micro-scale interface problem in Sec. 2.2 we apply an upscaling approach. To do so we need to establish a relation between the macro-scale and the micro-scale.

In the following, we denote the solution of the zeroth-order model in Sec. 2.1 as $u^0 = (\rho^0, \mathbf{v}^0, E^0)$, the solution of the micro-scale interface problem in Sec. 2.2 as $u^\varepsilon = (\rho^\varepsilon, \mathbf{v}^\varepsilon, E^\varepsilon)$ and the solution of the effective model in Sec. 2.3 as $u^{eff} = (\rho^{eff}, \mathbf{v}^{eff}, E^{eff})$.

Let $\bar{\mathbf{x}}_C \in \Gamma_{Int}$ characterize the position of one injection channel in Ω_{HG}^ε as introduced in the micro-scale interface problem, see Figure 4(a). Then the roughness domain $R(\bar{\mathbf{x}}_C)$ consists of the injection channel itself and the free flow on top of this channel, see Figure 4(a). We introduce the transformation $\mathcal{Y}_{\bar{\mathbf{x}}_C} : R(\bar{\mathbf{x}}_C) \rightarrow Y$ that relates each roughness element $R(\bar{\mathbf{x}}_C)$ on the macro-scale

$$\mathcal{Y}_{\bar{\mathbf{x}}_C}(\mathbf{x}) := \frac{\mathbf{x} - \bar{\mathbf{x}}_C}{\varepsilon}, \quad \forall \mathbf{x} \in R(\bar{\mathbf{x}}_C) \quad (3.1)$$

to the cell domain $Y := \{\mathbf{y}(\mathbf{x}) = \mathcal{Y}_{\bar{\mathbf{x}}_C}(\mathbf{x}), \mathbf{x} \in R(\bar{\mathbf{x}}_C)\}$ on the micro-scale as shown in Figure 4(b).

3.1. Upscaling

To account for micro-scale effects at the interface Γ_{Int} we use an upscaling strategy. For this purpose we approximate the micro-scale interface solution u^ε with an asymptotic

expansion in terms of powers of ε :

$$u^\varepsilon(\mathbf{x}) = u^0(\mathbf{x}) + \varepsilon u^1(\mathbf{x}, \mathbf{y}(\mathbf{x})) + \mathcal{O}(\varepsilon^2), \quad \forall \mathbf{x} \in R(\bar{\mathbf{x}}_C). \quad (3.2)$$

Here, u^0 is the *non-dimensionalized* solution of the zeroth-order problem, where the roughness is not modeled. The goal of the term εu^1 is therefore to address the roughness. Following [14], we assume that the upscaling function u^1 depends on the macro-scale variable \mathbf{x} and the micro-scale variable \mathbf{y} by

$$u^1(\mathbf{x}, \mathbf{y}(\mathbf{x})) := \zeta_{\bar{\mathbf{x}}_C} \left(\frac{\mathbf{x} - \bar{\mathbf{x}}_C}{\varepsilon} \right), \quad \forall \mathbf{x} \in R(\bar{\mathbf{x}}_C). \quad (3.3)$$

Here, the so-called cell functions $\zeta_{\bar{\mathbf{x}}_C} = (\chi, \phi, \pi)$ are assumed to be sufficiently smooth functions in the cell domain Y .

3.2. Cell problem

To determine the upscaling function u^1 we derive a problem on the cell domain Y . For this purpose, we consider an arbitrary but fixed roughness element $R(\bar{\mathbf{x}}_C)$. Because of the pore scale we assume the flow to be laminar. Thus, on $R(\bar{\mathbf{x}}_C)$ the flow within the injection channel and the free flow above can be described using the *dimensionless* Navier-Stokes equations:

$$\begin{aligned} (\mathbf{v} \cdot \nabla) \rho + \rho \nabla \cdot \mathbf{v} &= 0, \\ (\mathbf{v} \cdot \nabla) \mathbf{v} + \frac{1}{\rho} \nabla p - \frac{1}{\rho Re} \nabla \cdot \boldsymbol{\tau} &= \mathbf{0}, \\ (\mathbf{v} \cdot \nabla) p + \gamma p (\nabla \cdot \mathbf{v}) - \frac{\gamma - 1}{Re} ((\boldsymbol{\tau} \cdot \nabla) \mathbf{v} - \nabla \cdot \mathbf{q}) &= 0. \end{aligned} \quad (3.4)$$

To analyze the subsonic and steady state flow we switch to primitive variables, i.e., $u = (\rho, \mathbf{v}, p)$. The stress tensor $\boldsymbol{\tau}$ and the heat flux \mathbf{q} are defined by

$$\boldsymbol{\tau} = -\frac{2}{3} \mu (\nabla \cdot \mathbf{u}) I + \mu (\nabla \mathbf{u} + (\nabla \mathbf{u})^T), \quad \mathbf{q} = -c_p \frac{\mu}{Pr} \nabla T, \quad (3.5)$$

with the identity matrix I , the Prandtl number Pr , the dynamic viscosity μ and the heat capacity c_p . The dimensionless ideal gas law $p = \rho T$ is used to close the system.

Plugging the asymptotic expansion (3.2) and the upscaling function (3.3) into (3.4) and neglecting higher order terms, for details see [14], we obtain the following *dimensionless* system of equations

$$\begin{aligned} (\mathbf{v}^0 \cdot \nabla_y) \phi(\mathbf{y}) + \rho^0 \nabla_y \cdot \boldsymbol{\chi}(\mathbf{y}) &= 0, \\ \rho^0 (\mathbf{v}^0 \cdot \nabla_y) \boldsymbol{\chi}(\mathbf{y}) + \nabla_y \pi(\mathbf{y}) &= \frac{\mu}{\varepsilon Re} (\Delta_y \boldsymbol{\chi}(\mathbf{y}) + \frac{1}{3} \nabla_y (\nabla_y \cdot \boldsymbol{\chi}(\mathbf{y}))), \\ (\mathbf{v}^0 \cdot \nabla_y) \pi(\mathbf{y}) + \gamma p^0 \nabla_y \cdot \boldsymbol{\chi}(\mathbf{y}) &= \frac{\gamma}{\varepsilon Re} \frac{c_p \mu}{Pr} \left(\frac{1}{\rho^0} \Delta_y \pi(\mathbf{y}) - \frac{p^0}{(\rho^0)^2} \Delta_y \phi(\mathbf{y}) \right), \end{aligned} \quad (3.6)$$

for $\mathbf{y} \in Y$, where $\boldsymbol{\chi}$, ϕ , π are the upscaling functions corresponding to velocity \mathbf{v} , density ρ and pressure p , respectively. We emphasize that the zeroth-order solution u^0 enters the system (3.6). It depends on the macro-scale, i.e., $u^0(\mathbf{x}(\mathbf{y})) = u^0(\mathcal{Y}_{\bar{\mathbf{x}}_C}^{-1}(\mathbf{y})) = u^0(\bar{\mathbf{x}}_C + \varepsilon \mathbf{y})$. For $y_2 \geq 0$ the solution u^0 is determined from Ω_{HG} and for $y_2 < 0$ from the Darcy-based porous medium model on Ω_{PM} , see Fig. 1. For each fixed $\bar{\mathbf{x}}_C$, the macro-scale solution is assumed to be constant in y_1 direction, but it varies in y_2 . The roughness is assumed to be periodic, i.e.,

$$\boldsymbol{\chi}, \phi, \pi \text{ periodic on } \Gamma_p. \quad (3.7)$$

Note that on Γ_W the boundary condition is chosen to ensure no-slip conditions for the

micro-scale interface problem

$$\mathbf{v}^\varepsilon = \mathbf{v}^0 + \varepsilon \mathbf{v}^1 \equiv \mathbf{v}^0 + \varepsilon \boldsymbol{\chi} = \mathbf{v}^0 + \varepsilon \left(-\frac{\mathbf{v}^0}{\varepsilon} \right) = \mathbf{0}. \quad (3.8)$$

Furthermore, with the assumption of constant pressure $p^\varepsilon = p^0$, we ensure isothermal walls $T^\varepsilon = T_s^0$ for Γ_W , because

$$\rho^\varepsilon = \rho^0 + \varepsilon \phi = \frac{p^0}{T_f^0} + \varepsilon \left(\frac{(T_f^0 - T_s^0)p^0}{\varepsilon T_s^0 T_f^0} \right) = \frac{p^0}{T_s^0}. \quad (3.9)$$

On Γ_{Inj} , corresponding to $\Gamma_{f,\varepsilon}$, the injection of a Darcy-modeled velocity needs to be adjusted to the now resolved structures, i.e.,

$$\mathbf{v}^\varepsilon = \mathbf{V}^\varepsilon = \mathbf{v}^0 + \varepsilon \boldsymbol{\chi} = \mathbf{v}^0 + \varepsilon \left(\frac{\mathbf{v}^0}{\varepsilon} \left(\frac{1}{\varphi} - 1 \right) \right) = \frac{\mathbf{v}^0}{\varphi}. \quad (3.10)$$

The system (3.6) is closed by the following boundary conditions

$$\boldsymbol{\chi} = -\frac{\mathbf{v}^0}{\varepsilon}, \quad \phi = \frac{(T_f^0 - T_s^0)p^0}{\varepsilon T_s^0 T_f^0}, \quad \text{on } \Gamma_W, \quad (3.11)$$

$$\boldsymbol{\chi} = \frac{\mathbf{v}^0}{\varepsilon} \left(\frac{1}{\varphi} - 1 \right), \quad \phi = 0, \quad \text{on } \Gamma_{Inj}, \quad (3.12)$$

$$\left(\frac{\mu}{\varepsilon Re} \nabla_y \boldsymbol{\chi} - \pi \mathbf{I} \right) \mathbf{n}_y = \mathbf{0}, \quad \nabla_y \phi \cdot \mathbf{n}_y = 0, \quad \text{on } \Gamma_{up}. \quad (3.13)$$

The boundary conditions for Γ_{up} arise from the weak formulation of the cell problem.

The solution of the *dimensionless* system (3.6) with the boundary conditions (3.7), (3.11), (3.12) and (3.13) is used to determine effective constants by:

$$\begin{aligned} \langle \chi_1 \rangle &:= \frac{1}{|\Gamma_{Int}|} \int_{\Gamma_{Int}} \chi_1 dy, \quad \langle \chi_2 \rangle := \frac{1}{|\Gamma_{Int}|} \int_{\Gamma_{Int}} \chi_2 dy, \\ \langle \phi \rangle &:= \frac{1}{|\Gamma_{Int}|} \int_{\Gamma_{Int}} \phi dy, \quad \langle \pi \rangle := \frac{1}{|\Gamma_{Int}|} \int_{\Gamma_{Int}} \pi dy. \end{aligned} \quad (3.14)$$

3.3. Effective boundary conditions

In Sec. 2.3 effective boundary conditions are used at the interface Γ_{Int} . These boundary conditions are determined using the effective constants (3.14) that are derived in Sec. 3.2 solving the cell problem. Applying the upscaling strategy presented in Sec. 3.1 the effective velocity is computed as follows

$$\mathbf{v}^{eff} = \mathbf{v}^0 + \varepsilon \langle \boldsymbol{\chi} \rangle. \quad (3.15)$$

Note that now all quantities derived from solving the dimensionless cell problem are multiplied with non-dimensionalized reference quantities. To ensure the correct cooling gas mass flow rate we only consider the injection velocity v_2 . Since on top of the interface, i.e., $x_2 > 0$, the flow is dominated by the inflow of the cooling gas in wall normal direction, we neglect the influence of the streamwise velocity on the hot gas flow to determine the cooling gas inflow rate. For the cooling gas mass flow rate to be consistent in the zeroth-order problem as well as in the effective problem, we need

$$v_2^0 \rho^0 = \frac{\dot{m}_c}{A_c} = v_2^{eff} \rho^{eff} = (v_2^0 + \varepsilon \langle \chi_2 \rangle) \frac{p_{HG}}{R T^{eff}}$$

or, equivalently,

$$T^{eff} = (v_2^0 + \varepsilon \langle \chi_2 \rangle) \frac{p_{HG} A_c}{R \dot{m}_c} = v_2^0 \frac{p_{HG}}{R v_2^0 \rho^0} + \varepsilon \langle \chi_2 \rangle \frac{p_{HG} A_c}{R \dot{m}_c}.$$

Here, the pressure p_{HG} corresponds to the pressure of the attached hot gas flow field at the interface. Since this pressure is not significantly affected by the coupling, i.e., it remains constant with $p_{HG} = p^0$, the effective temperature is determined by

$$T^{eff} = T^0 + \varepsilon \langle \chi_2 \rangle \frac{p_{HG} A_c}{R \dot{m}_c}. \quad (3.16)$$

Note that T^{eff} tends to T^0 for $\varepsilon \rightarrow 0$, i.e., the effective boundary condition is consistent with the boundary conditions of the zeroth-order problem.

4. Numerical results

In this section, we analyze numerical results of transpiration cooling simulations using effective boundary conditions. These are compared to coupled simulations using the two-domain approach (zeroth-order problem) partly presented in [23]. For this purpose, the experimental setup for the investigation of the turbulent channel flow and the characteristics of the porous material, respectively, are briefly described in Sec. 4.1, followed by the numerical setup in Sec. 4.2. Then we first discuss the numerical results for the zeroth-order problem, see Sec. 4.3. From these simulations we extract data that enter the cell problem. The results of the latter are discussed in Sec. 4.4. In Sec. 4.5 we perform computations with effective boundary conditions and compare these results with uniform and non-uniform transpiration cooling results.

4.1. Experimental setup

For our coupled simulation, we use a setup corresponding to the experiments described in [24, 25]. Here, a porous carbon composite sample is mounted into the sidewall of a subsonic wind tunnel. On the backside of the porous material, a coolant reservoir is attached. This experimental setup is shown in Fig. 5. The test section is 1.32 m long with the porous material beginning 0.58 m downstream of the entrance, the height is 90 mm and the width 60 mm . The porous wall sample measures $61\text{ mm} \times 61\text{ mm}$ and is 15 mm thick. The flow conditions in the hot gas channel (air) and for the cooling gas (air) for this configuration are listed in Tab. 1. Parameters of the porous material are recorded in Tab. 2. Note that the heat transfer coefficient h_v can only be estimated and not measured.

4.2. Numerical setup

For first investigations we do not consider the three-dimensional experimental setup but perform 2D computations in the cross-section of the 3D configuration along the center-line in streamwise direction of the hot gas flow. Following [23], we first run a coupled simulation of the zeroth-order problem with uniform injection, where we perform alternately computations with a flow solver in the hot gas domain $\Omega_{HG} = [0; 1.32] \times [0; 0.06]$ and a porous medium solver in the porous medium domain $\Omega_{PM} = [0.58; 0.641] \times [-0.015; 0]$. At the interface data are exchanged according to the coupling conditions (2.23)-(2.26). The flow solver Quadflow [26] solves the RANS equations (2.1)-(2.5) iteratively by using a fully adaptive cell-centered finite volume method on locally refined grids. For the

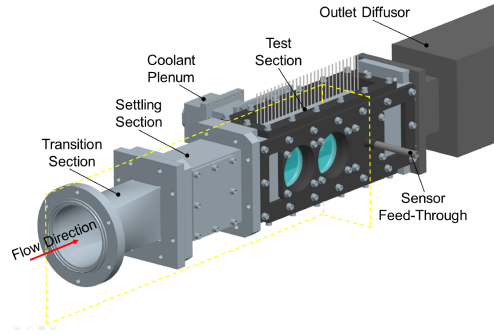


FIGURE 5. Experimental setup for turbulent hot gas channel flow by Langener et al. [24].

| | | |
|-------------------------|----------------------|-----------------------|
| Mach number | M_∞ | 0.3 |
| density | ρ_∞ | 0.78 kg/m^3 |
| temperature | T_∞ | 425 K |
| pressure | p_∞ | $95,200 \text{ Pa}$ |
| turbulence intensity | Tu_∞ | 0.5% |
| viscosity ratio | $(\mu_t/\mu)_\infty$ | 0.001 |
| isentropic exponent | γ | 1.4 |
| Prandtl number | Pr | 0.72 |
| blowing ratio | F | 0.24% |
| coolant mass flow rate | \dot{m}_c | 0.875 g/s |
| reservoir pressure | p_R | $334,000 \text{ Pa}$ |
| coolant reservoir temp. | T_c | 304.2 K |
| backside temperature | T_b | 321.9 K |

TABLE 1. Flow parameters.

| | | |
|---------------------------|-------------------------|-----------------------------------|
| through flow direction | | parallel |
| porosity | φ | 0.111 |
| heat conductivity (par) | $\kappa_{s,\text{par}}$ | 15.1856 W/(mK) |
| heat conductivity (nor) | $\kappa_{s,\text{nor}}$ | 1.5748 W/(mK) |
| permeability | K_D | $3.57 \cdot 10^{-13} \text{ m}^2$ |
| Forchheimer coefficient | K_F | $5.17 \cdot 10^{-8} \text{ m}$ |
| heat transfer coefficient | h_v | $10^6 \text{ W/(m}^3\text{K)}$ |

TABLE 2. Porous medium parameters.

porous medium flow a finite element solver has been implemented using the deal.II library [27].

The hot gas flow solver on Ω_{HG} is initialized on a coarse grid that comprises 108,000 grid cells. The grid lines are concentrated towards the walls using a stretching function. The final adaptive grid after 14 coupling iterations and, hence, adaptations consists of about 770,000 grid cells. The porous material Ω_{PM} is discretized by a uniform grid with 306×65 grid cells. No adaptation is used in the porous medium domain. The grid lines are concentrated towards the hot gas interface.

For a first investigation, nine positions in the hot gas and the porous medium domain

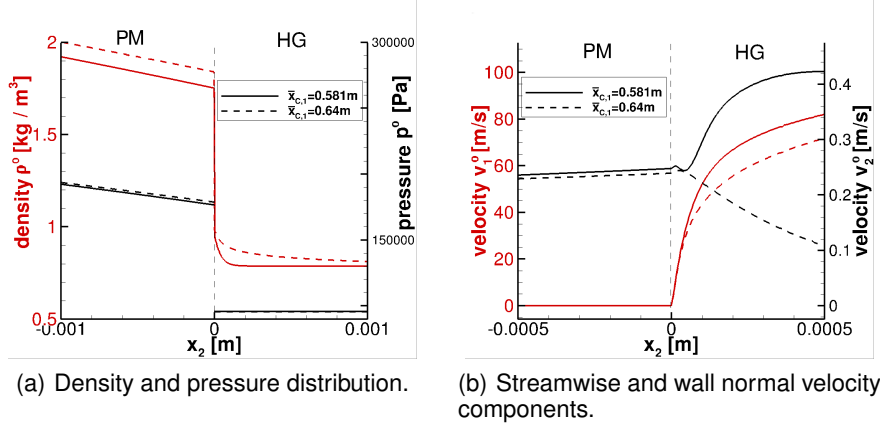


FIGURE 6. Zeroth-order problem: porous medium and hot gas information near the interface in wall normal direction.

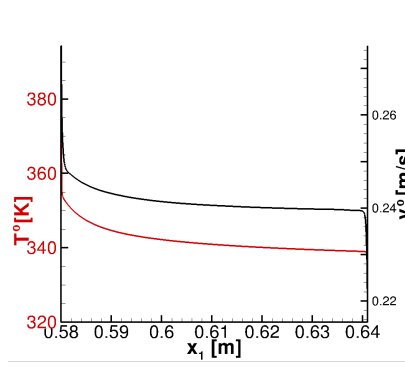


FIGURE 7. Zeroth-order problem: temperature and injection velocity along the interface.

are chosen at which the zeroth-order solution is used as input parameter for the computation of nine corresponding cell problems that are solved by a finite element method again using the deal.II library [27]. The grid for the cell problem consists of 8,400 grid cells. By using the permeability constant K_D from Tab. 2 and the Ergun approach (2.28) we get a solid wall diameter $d_S = 1.759 \times 10^{-4}$ m and therefore one micro-scale element of the size $\varepsilon = 1.979 \times 10^{-4}$ m. The effective coefficients derived from the solutions of the cell problems are interpolated linearly to cover the entire interface.

Subsequently, the flow solver Quadflow [26] is used to solve the effective problem on Ω_{HG} . Here, the coarse grid for the flow solver starts with 522,000 grid cells. Since the boundary conditions (3.15) and (3.16) depend on the zeroth-order solution along the interface, we resolve the grid at the interface to the level of the zeroth-order computation to ensure matching cell interfaces.

4.3. Zeroth-order problem

Simulations solving the zeroth-order problem (uniform injection) are performed. From these computations we extract data that enter the cell problem and the effective problem. Data extracted in wall normal direction at the interface Γ_{Int} are shown in Fig. 6(a) and 6(b). These enter the cell problem (3.6). Since these data depend on the position $\bar{x}_{C,1}$

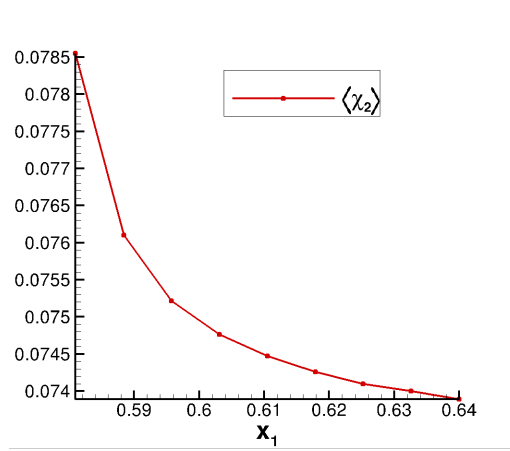


FIGURE 8. Cell problem: $\langle \chi_2 \rangle$ interpolated to cover the entire interface Γ_{Int} .

streamwise direction, we exemplarily present the extracted data for two positions $\bar{x}_{C,1} = 0.581m$ and $\bar{x}_{C,1} = 0.64m$ at the leading and trailing edge of the interface Γ_{Int} . We note a significant influence of the position on the density and the velocity components, especially in the hot gas flow.

The zeroth-order model does not impose pressure continuity across the interface from the surface of the porous medium to the hot gas channel. Solving the porous medium model without the two temperature equations, i.e. assuming a constant temperature through the medium, leads to pressure continuity and the correct mass flow rate. This indicates the correct solving of the transport system for the density and the velocity. For our model the correct mass flow rate entering the hot gas is ensured. Additionally, pressure continuity at the hot gas interface could be imposed by parameter fitting, e.g. the heat transfer coefficient, in the porous medium.

In Figure 7 we present the temperature as well as the injection velocity in the hot gas flow at the interface Γ_{Int} . These data are used in the effective boundary conditions (3.16) and (3.15) of the effective problem.

4.4. Cell problem results

Using the zeroth-order solution presented in Sec. 4.3, the data perpendicular to the hot gas flow direction are extracted at nine equidistant positions $\bar{x}_{C,1}$ along the interface, see dots in Fig. 8. With this information $(\rho^0, \mathbf{u}^0, p^0)$ for each of the points $\bar{x}_{C,1}$, one cell problem is solved. Exemplarily, in Fig. 9 the cell function solutions are presented for $\bar{x}_{C,1} = 0.6105$.

From the cell function solutions effective constants at Γ_{Int} according to (3.14) are derived for the nine reference points $\bar{x}_{C,1}$. Exemplarily, the interpolation of $\langle \chi_2 \rangle$ is presented in Fig. 8, because it enters the effective boundary conditions in (3.15) and (3.16). The decreasing behavior of this effective constant can be explained by the increase of the boundary layer thickness along the interface in the zeroth-order solution.

Justified by the low Reynolds number in the pore, the flow in the cell problem is assumed to be laminar. On the other hand, the zeroth-order solution for $y > 0$ is derived from a turbulent flow boundary layer. The derivation of effective constants of a turbulent cell problem could be feasible, see e.g. [28].

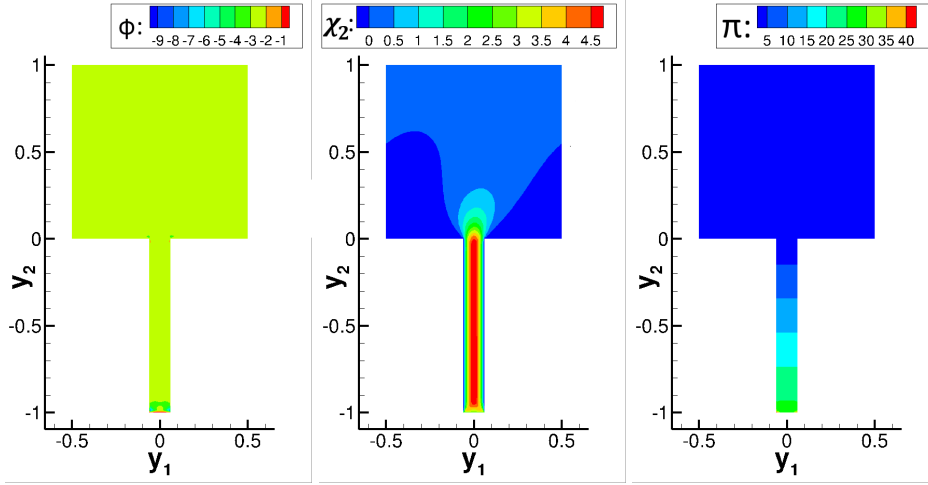


FIGURE 9. Cell problem: solution of the cell problem at $\bar{x}_{C,1} = 0.6105$ for ϕ , χ_2 and π .

4.5. Effective problem results

For the computation of the effective problem presented in Sec. 2.3 we need to determine the effective boundary conditions (3.15) and (3.16). Here, \mathbf{u}^0 and T^0 are determined by the solution of the zeroth-order problem presented in Fig. 7 at the interface. By linear interpolation we compute effective constants for the entire interface Γ_{Int} .

In Figure 10 the temperature and the wall-normal velocity distribution along the interface Γ_{Int} for the effective computation are presented. Note that there is no coupling with the porous medium. Similarly to the zeroth-order solution in Sec. 4.3 we observe the development of a cooling film and the thickening of the boundary layer resulting in a significant temperature drop along the interface Γ_{Int} . In particular, in the effective case the temperature drops to only 348 K instead of 340 K in the zeroth-order problem. Thus, the inhomogeneous injection caused by the micro-scale pores at the surface of the porous medium affects the cooling, i.e., the cooling process is less efficient than predicted by the zeroth-order solution.

To evaluate the effective model, the effective results have to be compared with the results obtained by a simulation of the micro-scale interface model. For the given 2D configuration we obtain $\varepsilon = 1.979 \times 10^{-4}\text{ m}$ by (2.27) and (2.28). Thus, the interface would consist of approximately 300 microscopic injection channels for the micro-scale interface problem presented in Sec. 2.2. Since resolving these would lead to an extremely fine grid, the computation of the micro-scale interface problem is too costly. Instead, we perform a coupled simulation with non-uniform injection realized by applying a sine function (with 300 periods) to a uniform velocity distribution, where the averaged value corresponds to the mass flow rate \dot{m}_c . Thus, there exist local regions with high inflow rates and regions with no inflow.

In Fig. 11 the temperature distribution at the interface for the uniform (representing the zeroth-order problem), the non-uniform (representing a micro-scale problem) and the effective case are compared. We observe that the cooling effect along the interface Γ_{Int} is strongest for the uniform injection and smallest for the non-uniform injection. Obviously, the effective injection clearly shows a better agreement with the non-uniform injection in comparison with the uniform injection. This is also reflected in the averaged temper-

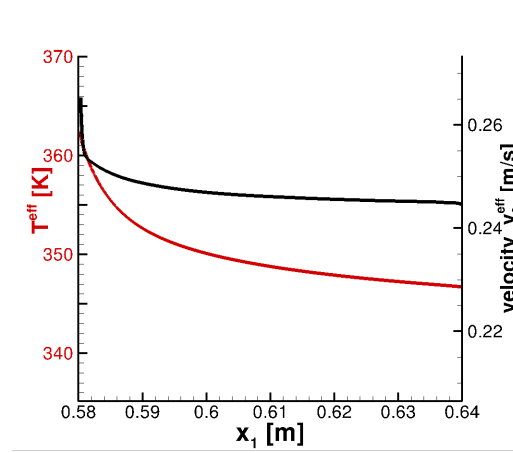


FIGURE 10. Effective problem: temperature (red) and wall-normal velocity (black) along the interface.

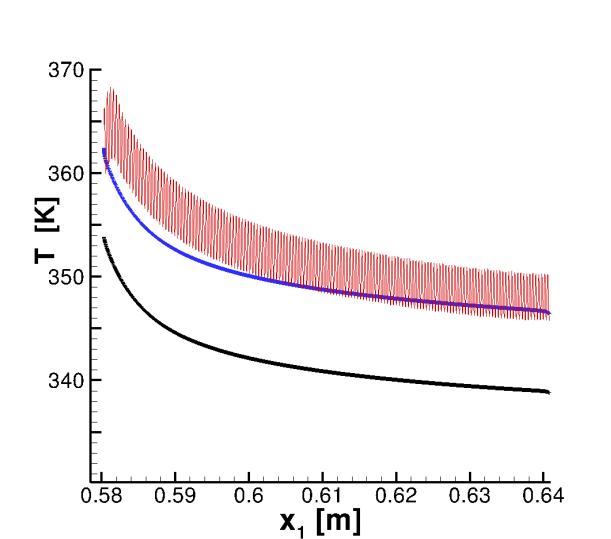


FIGURE 11. Temperature at the interface Γ_{Int} for the uniform(black), the non-uniform(red) and the effective (blue) case.

atures along the interface Γ_{Int} : $\bar{T}_{Int}^0 = 342 K$ for the uniform injection, $\bar{T}_{Int}^{sin} = 352 K$ for the non-uniform case and $\bar{T}_{Int}^{eff} = 350 K$ for the effective simulation.

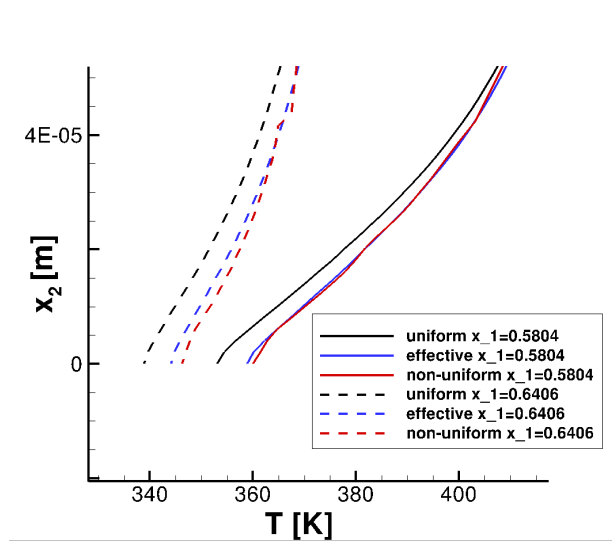
This trend can also be seen in the cooling efficiency η that can be determined by relating the averaged temperature \bar{T}_{Int} along the interface Γ_{Int} to the inflow hot gas temperature T_{HG} and the reservoir cooling gas temperature T_C as follows

$$\eta = \frac{\bar{T}_{Int} - T_{HG}}{T_C - T_{HG}}.$$

The cooling efficiency along the porous material interface is summarized in Tab. 3 for the uniform, non-uniform and effective simulation. The lower cooling efficiency for non-uniform injection is caused by the larger wall temperature gradients. For this purpose we

| | uniform | non-uniform | effective |
|--------|---------|-------------|-----------|
| η | 0.687 | 0.604 | 0.621 |

TABLE 3. Cooling efficiency.

FIGURE 12. Temperature distribution in the boundary layer at positions $x_1 = 0.5804 m$ and $x_1 = 0.6406 m$.

present in Fig. 12 the temperature in the boundary layer for position $x_1 = 0.5804 m$ and $x_1 = 0.6406 m$ for the uniform, the non-uniform and the effective computation. Close to the wall, i.e., $x_2 = 0$, the temperature gradient increases for uniform, effective and non-uniform injection. Again, the effective result better catches the trend of the non-uniform result than the uniform one. This holds true for both positions, the leading edge and the trailing edge of the interface Γ_{Int} .

5. Conclusions

We present an effective model that simulates transpiration cooling taking micro-scale effects into account without resolving micro-scale pores. For this purpose we use an upscaling strategy consisting of three steps:

- (i) we solve a coupled zeroth-order problem of the hot gas flow and the porous medium flow with uniform mass injection at the interface;
- (ii) motivated by an asymptotic expansion a cell problem is derived on the micro-scale that depends on the data of the coupled computation;
- (iii) an effective problem is solved in the hot gas channel with effective boundary conditions at the interface using averaged data from the cell problems and extracted data from the coupled problem (uniform injection).

Numerical computations show that the cooling efficiency is reduced when using a non-uniform injection in comparison to a uniform injection. This effect is reflected in the

effective computation. Thus, the effective model provides a better approximation than the coupled problem with uniform injection.

Acknowledgments

Financial support has been provided by the German Research Foundation (Deutsche Forschungsgemeinschaft – DFG) in the framework of the Sonderforschungsbereich Transregio 40.

References

- [1] LINN, J. AND KLOKER, M.J. (2008). Numerical investigations of film cooling and its influence on the hypersonic boundary-layer flow. In: Gülhan, A. (Ed.), *RESPACE - Key Technologies for Reusable Space Systems, NNFM*, vol. 98. Springer, 151–169.
- [2] LINN, J. AND KLOKER, M.J. (2011). Effects of wall-temperature conditions on effusion cooling in a Mach-2.67 boundary layer. *AIAA Journal*, **49**(2), 299–307.
- [3] LINN, J., KELLER, M. AND KLOKER, M.J. Effects of inclined blowing on effusion cooling in a Mach-2.67 boundary layer. Annual Report SFB TRR40 2010. Munich.
- [4] SELZER, M., LANGENER, T., HALD, H. AND V. WOLFERSDORF, J. Production and characterization of porous C/C material. Annual Report SFB TRR40 2009. Munich.
- [5] ORTELT, M., HALD, H., HERBERTZ, A. AND MÜLLER, I. (2013). Advanced design concepts for ceramic thrust chamber components of rocket engines. In: *5th European Conference for Aeronautics and Space Sciences (EUCASS), Munich*.
- [6] HERBERTZ, A. AND SELZER, M. (2014). Analysis of coolant mass flow requirements for transpiration cooled ceramic thrust chambers. *Trans. JSASS Aerospace Tech. Japan*, **12**(29), 31–39.
- [7] JIANG, P., YU, L., SUN, J. AND WANG, Y. (2004). Experimental and numerical investigation of convection heat transfer in transpiration cooling. *Applied Thermal Engineering*, **24**, 1271–1289.
- [8] LIU, Y., JIANG, P., XIONG, Y. AND WANG, Y. (2013). Experimental and numerical investigation of transpiration cooling for sintered porous flat plates. *Applied Thermal Engineering*, **50**, 997–1007.
- [9] DAHMEN, W., GOTZEN, T., MÜLLER, S. AND ROM, M. (2014). Numerical simulation of transpiration cooling through porous material. *International Journal for Numerical Methods in Fluids*, **76**(6), 331–365.
- [10] DAHMEN, W., MÜLLER, S., ROM, M., SCHWEIKERT, S., SELZER, M. AND V. WOLFERSDORF, J. (2015). Numerical boundary layer investigations of transpiration-cooled turbulent channel flow. *International Journal of Heat and Mass Transfer*, **86**, 90–100.
- [11] KÖNIG, V., ROM, M., MÜLLER, S., SCHWEIKERT, S., SELZER, M. AND V. WOLFERSDORF, J. (2019). Numerical and experimental investigation of transpiration cooling with C/C characteristic outflow distributions. *Journal of Thermophysics and Heat Transfer*, **33**(2), 449–461.
- [12] YANG, L., MIN, Z., YUE, T., RAO, Y. AND CHYU, M.K. (2019). High resolution cooling effectiveness reconstruction of transpiration cooling using convolution modeling method. *International Journal of Heat and Mass Transfer*, **133**, 1134–1144.
- [13] YANG, G., COLTMAN, E., WEISHAUP, K., TERZIS, A., HELMIG, R. AND WEIGAND, B. (2019). On the Beavers–Joseph interface condition for non-parallel

- coupled channel flow over a porous structure at high Reynolds numbers. *Transport in Porous Media*, **128**(2), 431–457.
- [14] DEOLMI, G., DAHMEN, W. AND MÜLLER, S. (2017). Effective boundary conditions: a general strategy and application to compressible flows over rough boundaries. *Communications in Computational Physics*, **21**(2), 358–400.
- [15] ACHDOU, Y., PIRONNEAU, O. AND VALENTIN, F. (1998). Effective boundary conditions for laminar flows over periodic rough boundaries. *Journal of Computational Physics*, **147**, 187–218.
- [16] JÄGER, W. AND MIKELIC, A. (2009). Modeling effective interface laws for transport phenomena between an unconfined fluid and a porous medium using homogenization. *Transport in Porous Media*, **78**(3), 489–508.
- [17] CARRARO, T., GOLL, C., MARCINIAK-CZOCZRA, A. AND MIKELIC, A. (2015). Effective interface conditions for the forced infiltration of a viscous fluid into a porous medium using homogenization. *Computational Methods in Application of Mechanical Engineering*, **292**, 195–220.
- [18] LACIS, U. AND BAGHERI, S. (2017). A framework for computing effective boundary conditions at the interface between free fluid and a porous medium. *Journal of Fluid Mechanics*, **812**, 866–889.
- [19] WILCOX, D.C. (2006). Turbulence Modeling for CFD. *DCW Industries Inc., 3rd edition*.
- [20] WHITE, F.M. (2009). *Fluid Mechanics*. McGraw-Hill.
- [21] NIELD, D.A. AND BEJAN, A. (2006). *Convection in Porous Media*. Springer. 3rd ed.
- [22] ERGUN, S. (1952). Flow through packed columns. *Chemical Engineering Progress*, **48**(2), 89–94.
- [23] DAHMEN, W., KÖNIG, V., MÜLLER, S. AND ROM, M. (2017). Numerical investigation of transpiration cooling with uniformly and non-uniformly simulated injection. In: *7th European Conference for Aeronautics and Space Sciences (EUCASS), Milan*.
- [24] LANGENER, T., v. WOLFERSDORF, J., SELZER, M. AND HALD, H. (2012). Experimental investigations of transpiration cooling applied to C/C material. *International Journal of Thermal Sciences*, **54**, 70–81.
- [25] SCHWEIKERT, S., v. WOLFERSDORF, J., SELZER, M. AND HALD, H. (2013). Experimental investigation on velocity and temperature distributions of turbulent cross flows over transpiration cooled C/C wall segments. In: *5th European Conference for Aeronautics and Space Sciences (EUCASS), Munich*.
- [26] BRAMKAMP, F., LAMBY, P. AND MÜLLER, S. (2004). An adaptive multiscale finite volume solver for unsteady and steady state flow computations. *Journal of Computational Physics*, **197**(2), 460–490.
- [27] BANGERTH, W., HARTMANN, R. AND KANSCHAT, G. (2007). deal.ii - a general-purpose object-oriented finite element library. *ACM Transactions on Mathematical Software*, **33**(4), 24/1–24/27.
- [28] DEOLMI, G., DAHMEN, W., MÜLLER, S., ALBERS, M., MEYSONNAT, P. AND SCHRÖDER, W. (2018). Effective boundary conditions for turbulent compressible flows over a riblet surface. *Theory, Numerics and Applications of Hyperbolic Problems I: Aachen, Germany, August 2016*, **236**, 473–485.